COMPARISON OF CURRENTS PREDICTED BY NASCAP/LEO MODEL SIMULATIONS AND ELEMENTARY LANGMUIR-TYPE BARE PROBE MODELS FOR AN INSULATED CABLE CONTAINING A SINGLE PINHOLE

Joel T. Galofaro
NASA Lewis Research Center

ABSTRACT

The behavior of a defect in the insulation of a short biased section of cable in a Low Earth Orbital (LEO) space environment is examined. Such studies are of the utmost importance for large space power systems where great quantities of cabling will be deployed. An insulated probe containing a pinhole is placed into a hypothetical high-density LEO plasma. The NASA Charging Analyzer Program (NASCAP/LEO) is used to explore sheath growth about the probe as a function of applied voltage and to predict I-V behavior. A set of independent current calculations using Langmuir's formulations for concentric spheres and coaxial cylinders are also performed. The case of concentric spheres is here extended to include the case of concentric hemispheres. Several simple Langmuir-type models are then constructed to bracket the current collected by the cable. The space charge sheath radius and impact parameters are used to determine the proper current regime. I-V curves are plotted for the models and comparisons are made with NASCAP/LEO results. Finally NASCAP/LEO potential contours and surface cell potential plots are examined to explain interesting features in the NASCAP/LEO I-V curve.

INTRODUCTION

Current collection by a partially insulated probe has been a long standing area of study in many spacecraft/plasma interaction processes. All spacecraft incorporate a large number of dielectric surfaces for thermal control, e.g. shuttle heat tiles, and for electrical power generation, e.g. solar cell arrays. Large dielectric surfaces can be differentially charged along their length because of locally variable incident charged particle fluxes. Staskus [1983], for example, has observed arc discharging between the 15 cm and 20 cm square tiles from the Space Shuttle Thermal Protection System exposed to monoenergetic multi-KeV electron beams.

Exposed conducting surfaces present quite a different problem in spacecraft charging, especially at the interfaces between adjacent insulator/conductor surfaces. Here, for example, Snyder [1983] observed arcing between fused silica cover slides and silver interconnects that were biased between -500 VOLTS and -1400 volts.

Conductors can either be biased or floated with respect to the spacecraft floating potential. Floating conductors are uninteresting because they tend to charge only to a negative potential of a few kT,

with respect to the plasma potential. This is due to the difference in the mobility of each charge species present; electrons possess a much greater mobility than ions by virtue of their lower atomic mass. Conductors biased with respect to spacecraft ground, by contrast, act as current sinks, creating field intensive regions which promote the collection of large currents.

All space plasmas have a tendency to remain electrically neutral. A slight imbalance in the space charge density gives rise to strong electrostatic forces which act to restore electrical neutrality in the plasma. In regions where the space plasma is subjected to strong electric fields, the plasma will attempt to readjust its charge distribution to shield itself from the field by forming a charge sheath. It should be evident that all spacecraft are intimately coupled to their plasma environment.

BACKGROUND

A striking phenomenon, that has been a subject of great interest, is the high currents collected through a pinhole in the dielectric covering a charged metal. Sullen, et al. [1969], evidently was the first to report of such an instance. This appears to have triggered a number of other papers looking into the same phenomenon, among which are those by Grier and McKinzie [1971], Kennerud [1974], Stevens [1978] and, Meulenberg and Robinson [1980].

Floating potential is measured with respect to a fixed potential in space called the plasma potential. The net current to a probe at its floating potential is zero [Reitz, 1969]. Therefore, a necessary condition for currents to be collected through a pinhole in a dielectric material is that the bias voltage of the substrate must not be equal to the floating potential. Hereafter, I will call the substrate bias exposed by the pinhole the pinhole bias. If the bias voltage is allowed to go slightly negative of the floating potential, electrons will start to be repelled, and the net current collected through the pinhole will be due to ions. If the pinhole bias is made negative enough, the number of collected ions will become saturated, and only the ion current density Ji will be collected, resulting in a positive charge sheath. Alternatively, if the pinhole bias is allowed to go slightly positive to that of the floating potential, ions will start being repelled and more electrons than ions will be collected by the pinhole. If the pinhole bias is increased just past that of the plasma potential, the ions will redistribute themselves away from the immediate vicinity of the pinhole. A negative charge sheath will form, and the electron current density Je will be collected by the pinhole. Finally, if the pinhole bias is made even more positive, the pinhole will exhibit a rather complicated current-voltage relationship, depending on the constituency and the bulk properties of the plasma.

Sudden sheath growth about a pinhole that is biased significantly above or below the plasma potential is often attributed to the onset of secondary electron emission [Katz, et al., 1977; Stevens, 1978]. Because charged particles entering the sheath region are subject to motion constraints imposed on them by their own angular momentum electric field, a certain percentage of them will miss the pinhole completely and strike the dielectric at a nearby point. If the

energy of the particle upon collision is above a certain energy threshold (determined by the bulk properties of the dielectric) and below a certain energy maximum, there is a high probability that more than one secondary electron will be liberated from the surface of the dielectric, causing the dielectric to charge positive. As the pinhole bias is increased, so too does the effective collecting area of this sheath, causing a yet greater number of high energy charged particles to enter the pinhole sheath region. As a result, more and more secondary electrons will be liberated causing a positive surface charge sheath to form on the dielectric. This phenomenon will henceforth be called "snapover."

With the new era of space exploration before us, the advent of Space Station Freedom, and TSS-1 Electrodynamic Tether applications, large amounts of insulated electrical cabling will be deployed in the construction and operation of these missions. Of increasing importance is the question of how such cables will perform in space, and, specifically here, how defects in the insulation might influence the behavior of a long insulated wire.

The present work will attempt to look into these issues by making use of a theoretical charging analyzer computer program (for low earth orbit) developed for NASA, called NASCAP/LEO. An insulated probe of appropriate geometry, containing a single pinhole, is defined and hypothetically placed into a known space environment. The code will then be used to explore sheath growth around the probe as a function of potential. Next, a bare cylindrical probe model will be presented and the I-V curves obtained by it plotted for comparison against those obtained by the NASCAP/LEO. Finally, a means of calculating the current collected by a spherical and a hemispherical probe, each having the same effective area as that of the pinhole, will be presented. These results will then be compared to the current collected by the pinhole as obtained from the NASCAP/LEO.

PROCEDURE

NASCAP/LEO is a finite element computer code designed expressly for the study of the electrostatic interaction between a spacecraft having charged surfaces and a cold dense plasma. Environmental parameters under NASCAP/LEO are user-specified parameters that need to be input prior to the calculation. Surface cell currents and potentials are particularly sensitive to the environment, and so some thought must be given to accurately describe the plasma environment for the model in question. The plasma environmental parameters used here and for all subsequent runs were based on typical high-density (worst case) LEO plasmas. (Plasma density was set at 10^{12}m-3, electron temperature at 0.1 eV, ion mass was set to 2.656 x 10^{-26} kg for oxygen ions, and the sheath boundary potential was set at 0.0873 eV.) NASCAP/LEO allows the user to specify the object geometry, material composition of conductors and insulators, conductor biases, scale size, and the placement of the object to be modeled in the NASCAP/LEO primary grid space.

The object modeled consisted of a short section of a copper conductor covered by a thin Kapton insulating jacket. A single puncture through the insulated jacket exposed a small area of the

underlying conductor. (NOTE: The surface area of the pinhole is much smaller than the surface area of the object.) The conductor was then biased in the code positively with respect to the plasma potential, while all the Kapton insulating surfaces were allowed to float. Initially, the insulating surfaces (for low conductor biases) were predicted to sit at a small negative potential relative to the plasma, and then to become more and more positive as the conductor bias increases. It was possible to keep track of how the charge sheath should propagate over the insulator surfaces, by looking at all insulator surface potentials over a range of varying conductor biases between 1 and 1000 volts.

Typical outputs from NASCAP/LEO consisted of 2-D potential contour plots (YZ and XY views) in the space around the object at a given conductor bias, as defined in the primary grid computational space. Other types of numerical outputs for individual surface cells were also obtained. These consisted of surface cell number and surface cell potential and current at each given conductor bias. By adding up the individual currents going to each surface cell, the incident total current collected by the object can be obtained. The total incident current to the object was then plotted versus the conductor bias to obtain the object's I-V curve characteristics.

In order to verify NASCAP/LEO results, several comparisons were made. The first of these comparisons involved the application of Langmuir's space charge limited current (SCLC) equation for parallel plates [Langmuir and Blodgett, 1924] (appendix D, eqs. 1.a and 1.b) and his SCLC equation for bare coaxial cylinders [Langmuir and Blodgett, 1923; (appendix D. eq. 3.a2). Assuming both planar-[Mandell and Jongeward, 1985] and cylindrical-type charge sheaths, these equations were solved for the space charge sheath radius (SCSR); the thickness between: (1) the bare cylindrical probe and a planar charge sheath boundary (appendix D, eq. 1.c) and (2) for the space charge sheath thickness between the bare cylindrical probe and a coaxial cylindrical charge sheath boundary (appendix D, eq. 3.c). Such SCSR determinations are a necessary step in finding the proper type of current collection regime that applies.

The relevancy of performing the above calculations should be clarified. What is being attempted here is a direct and independent current calculation of the object previously defined under the NASCAP/LEO. These calculations are to be performed from "first principals," starting with Langmuir's formulations for the Space Charge Limited Current to a bare parallel plate, sphere, and cylinder. In order to understand how an insulated object with a pinhole collects current, we first need to understand how this current compares to a similar object of the same geometry and dimensions, but containing no insulating surfaces. Hence, we need to deal with bare probe equations. Secondly, because the NASCAP/LEO object defined is an idealized object (constructed from a finite number of cubes of the same size) due to code limitations, it lacks the true geometry we are trying to model. Consequently, rather than finding the current to a bare object of length L of square cross section, we choose to approximate it, instead, by calculating the current to a bare cylinder of length L, having a surface area approximately equal to the NASCAP/LEO defined object.

Whenever planar conditions are assumed, that is, the charge sheath is assumed to be locally parallel to each point on the

surface, then the problem reduces to finding the SCSR, R_O (i.e., that distance between a biased planar anode on the surface of the object and a parallel charge sheath boundary). Fortunately, this problem is amenable to the type of solution Langmuir used for finding the maximum current between two biased parallel plates. [Mandell, M. J.; Jongeward, G. A., et al.] As a result, appendix D, eq. 1.c may be used to estimate the SCSR for a probe of any geometry.

The next set of comparisons involves calculating the Space Charge Limited Current collected by an insulated cylindrical probe containing a single pinhole. Because the pinhole contains the only exposed conductor on the surface of the object, it is the region where the largest currents will be collected, and so it is the logical choice of places to model. For simplicity, the model only considers conducting surfaces, leaving all insulator surfaces untreated. The assumption here is that the insulated portions of the probe will be at some small negative potential both far from and near to the pinhole if "snapover" type effects are not considered. As a result, only the exposed conducting area due to the pinhole was considered in the formulation of this model.

For the case of a pinhole, whose surface area is very small compared to the rest of the object, one would suppose current collection to be defined by a spherical or hemispherical geometry. As the scale size of the pinhole increases so that surface area of the pinhole becomes a more significant portion of the entire surface area, one would suppose current collection to be dependent upon the geometry of the exposed region.

The present paper will, therefore, attempt to calculate the the Space Charge Limited Current to an insulated conductor with a pinhole by employing both a bare conducting sphere and hemisphere, each having a surface area equal to the area of the pinhole. A close examination of the NASCAP/LEO object (appendix A, figure A-2) reveals the appropriate scale dimensions in the pinhole region. Appendices B and C show the calculations used to find the radius of a sphere and hemisphere of equal surface area to the pinhole. In the hemispherical case where we use a slightly larger probe radius, we use Langmuir's spherical form of the equation for the current (appendix D, eq. 4.a2), and cut the collected current in half (eq. 4.a1). This is equivalent to doubling the surface area of the hemisphere so that we are effectively collecting current from a larger spherical geometry probe from which we only accept half of the current. The comparisons here involve the application of Langmuir's SCLC equations for parallel plates (appendix D, eqs. 1.a and 1.b), Langmuir's SCLC equation for concentric spheres (appendix D, eq. 2.a2), and the subsequent derived expression for the SCLC equation for concentric hemispheres (appendix D, eq. 4.a2). Assuming both planar- and spherical-type charge sheaths for the bare spherical pinhole model, Langmuir's bare concentric sphere SCLC expression for the SCSR is solved for the thickness between: (1) a bare sphere and a locally parallel planar charge sheath boundary (appendix D, eq. 1.c) and (2) for the thickness between a bare sphere and a concentric spherical charge sheath boundary (appendix D, eq. 2.c). The last comparison assumes a hemispherical-type charge sheath for the bare hemispherical pinhole model. A solution is found for eq. 4.a2 in appendix D for the SCSR, the thickness between a bare hemispherical collector and a concentric hemispherical sheath

boundary (appendix D, eq. 4.c). After finding the SCSR for each case above, the applicable current collection regime was determined. Then I-V curves were plotted for each of the above pinhole models.

Appendix D, Table D-1 lists all the relevant equations cited previously. Although many of the equations compiled under this table can be readily obtained from a number of sources, to the best of this author's knowledge this appears to be the first time all pertinent equations have been presented in a single location. Because Langmuir's original work [Langmuir and Blodgett, 1923; Langmuir and Blodgett, 1923;] only extended over the cases of the parallel plates, coaxial cylinders, and concentric spheres, the concentric hemispherical equations presented in the table are newly derived. Fortunately, this was easily accomplished because the sphere and the hemisphere share the same geometry and only minor changes had to be incorporated into the case of Langmuir's concentric spheres to make them applicable to the hemispherical case. It should be noted that a minor error was found in Langmuir's expression for the current between concentric spheres [Langmuir & Blodgett, 1924]. His quoted parameters for D (for ions and electrons) could not be found, as stated, because of an inconsistency in the dimensions of his current equation. The error appears to have been propagated from the differences between the Gaussian and rationalized MKS units. Inclusion of a term for the permittivity of free space in the product of his current term rectifies the situation. All units for the equations in appendix D have been given in rationalized MKS so as to avoid any confusion as to which system is being used.

As stated previously, before any I-V curves can be calculated for the current collected by any of the geometries listed above, we first need to know which type of current collection regime applies at a given potential bias. I have already presented the calculations for one type of current collection regime, the space charge limited current regime. There is only one other type of current collection, the so-called orbit limited current regime, that can apply.

Whereas the space charge limited current is determined by the modification of the electric field near the sheath boundary (as a result of the space charge of electrons in that region), the orbit limited current collection is dominated by the orbital motion of electrons captured by the sheath. For the orbit limited case, the sheath radius is determined by the applied potential, the electron temperature, their angle of incidence upon entering the sheath and additionally the radius of the probe. Therefore electrons entering the sheath will either have: (1) too little energy to escape the sheath region and will end up striking the probe; or (2) they will have too great an energy to be captured, but due to their trajectory will still strike the probe; or (3) they will have too great an energy to be captured and will miss the probe completely leaving the sheath region altogether. The impact parameter is used to determine the sheath thickness for the orbit limited case.

Appendix E, eq. 5.0 defines the impact parameter. Table 2 gives us a means of calculating the type of current collection regime that applies at a given potential bias. Here, one first chooses the type of geometry he is interested in. Next, he calculates the space charge sheath radius for that geometry and the impact parameter and compares the two values obtained. When the space charge sheath radius is less than the impact parameter, a space charge limited

calculation holds. Equations 5.1a through 5.4a in table E-1 of appendix E are then used to calculate the current. When the impact parameter is less than the space charge sheath radius, an orbit limited calculation holds, and eqs. 5.1b through 5.4b may be used to estimate the collected current. Finally, when the space charge sheath radius is equal to the impact parameter and either set of formulations may be used for the current. This procedure outlined above is carried out for the range of potentials to be used in the NASCAP/LEO simulation. I-V curves are then obtained for direct comparisons with the NASCAP/LEO curve.

RESULTS

Figures f-1, f-2, f-3, f-4, and f-5 of appendix F show a comparison of the space charge sheath radius R_0 and the impact parameter P versus the applied voltage V for five different sheath thickness approximations. The first of these approximations (figure f-1) plots R_0,P versus V, using a planar type sheath approximation (appendix D, eq. 1.c) for R_0. The second type of approximation (figure f-2) uses a cylindrical sheath approximation (appendix D, eq. 3.c) for R_0. Figures f-3, f-4, and f-5 also plot R_0,P versus V but use planar (appendix D, eq. 1.c), spherical (appendix D, eq. 2.c), and hemispherical (appendix d, eq. 4.c) approximations respectively for the space charge sheath radius R_0.

It should be noted that the plots of R_0,P in figures f-1 through f-5 are dependent upon the particular probe geometry and the probe radius, a. The bare cylindrical probe models, which use a planar (figure f-1) and a cylindrical charge sheath thickness approximation (figure f-2) for R_0, have the same probe geometry and probe radius. Here the radius has been set equal to 1/2 the grid spacing (xmesh) used in the NASCAP/LEO object or a = 1.5875×10^{-3} meters. The spherical pinhole models, using planar (figure f-3) and spherical (figure f-4) space charge sheath thickness approximations for R_0, also use the same value for the probe radius a = 2.2391×10^{-4} meters determined from appendix B. The final hemispherical pinhole model uses a hemispherical charge sheath thickness approximation (figure f-5) for R_0 and uses the value of the probe radius a = 3.1666×10^{-4} meters, which is derived in appendix C.

Inspection of figures f-1 through f-5 show that R_0 is greater than P at any specified voltage along each of the curves. Therefore an orbit limited calculation is correct for all Langmuir-type probe models considered.

Figure f-6 (appendix f) shows a comparison of the currents collected by two different bare cylindrical probe models (curves e and f). Both of these models yield the same I-V curve. The same equation (appendix E, eq. 5.3b) is used to compute the current collected by both bare cylindrical probe models here. Referring back to figures f-1 and f-2 of appendix F, one can see that the range of values for R_0 varies considerably between the planar and cylindrical sheath thickness cases. One would, therefore, expect very different currents from each of these models were it not for the fact that neither of these sheath distances for R_0 is used in the current calculations for these models (since the orbit limited regime applies in both cases). Because each of these models uses the impact

parameter P (appendix E, eq. 5.0) in its current calculations, this leads to the same value of P at a given voltage and to the same I-V curve in both of these models. It should also be noted that the plots of V versus P in figures f-1 and f-2 are actually the same curve by virtue of eq. 5.0 in appendix E. (Because of the rescaling of the Y-axis dimension to the maximum value of R_o in each case, P is plotted accordingly.) Similarly, figures f-3 and f-4 of appendix F, also yield the same value for P for the reasons indicated above.

In figure f-6 of appendix F, curves a, b, and c show a comparison of the collected current between three different pinhole models. The resultant I-V curves are the same regardless of which of the probe models (spherical or hemispherical) is applied. What is also evident here is that the pinhole current collected by a bare spherical probe of equal surface area to that of the pinhole is about two orders of magnitude less than what would be collected by a non-insulated cylindrical probe of the same overall dimensions as the entire NASCAP/LEO object.

Consequently, the current collected by an insulated cylindrical probe containing a single pinhole has been bracketed. The actual current collected should fall somewhere between curves a, b, and c and curves e and f of figure 6 in appendix F. (Actually, one would suppose the collected current to be closer to curves a, b, and c, where the collecting surfaces are equal in area to that of the pinhole.)

Curve D in figure f-6 of appendix F shows the resultant I-V curves obtained from NASCAP/LEO runs for an insulated cylindrical probe containing a single pinhole. This curve contains many noteworthy features. Up to about 600-volts potential, the NASCAP/LEO curve appears to predict somewhat less current than either the spherical or hemispherical pinhole curves, although the current continues to converge to the 600-volt NASCAP/LEO current throughout this range. (It should also be noted that in the potential range, 25 volts through 115 volts, the current collected by the spherical and hemispherical pinhole models is approximately a factor of 4 greater than that predicted by the NASCAP/LEO model at any specified voltage within this range. The reason for this discrepancy will be explained in the conclusions.) In the range 130 volts to 600 volts, the current from the spherical, hemispherical pinhole models, and NASCAP/LEO curves appear to converge with one another. In the voltage range 620 volts to 680 volts, the spherical and hemispherical pinhole models collect nearly the same amount of current as predicted by the NASCAP/LEO simulation. In the potential range 685 volts to 1000 volts, the NASCAP/LEO curve appears to collect about a factor of 4 greater current than the spherical or hemispherical pinhole curves.

There are also several knee regions on the NASCAP/LEO curve where the current collection changes rather sharply. These regions occur between 100- and 130-volts, 600- to 640-volts, and 680- to 700-volts potential and can be attributed to the "snapover phenomenon."

The analysis begins by looking at NASCAP/LEO-generated contour plots of equipotentials and plots of surface cell potentials in each of the specified voltage regions above. The position of the zero-potential contour line, with respect to the pinhole, as well as changes in the insulator surface cell potentials will be used as an

indicator of the extent of the sheath edge or boundary. Thus drastic changes in the position of the sheath boundary should signal that "snapover" is occurring or has occurred.

Figures G-1(a) through G-8(a) of appendix G show a face on view of an x-z cutplane slicing through the pinhole. Figures G-1(b) through G-9(b) show a cross-sectional end on view of an x-y cutplane slicing through the pinhole. Figures G-1(c) through G-9(c) show a close-in view of the subdivided region, with all surface cells labeled and surface potentials plotted. Figures G-1(d) through G-9(d) show a full object view of the cable with all corresponding surface cell potentials and cell numbers plotted. For convenience, the plots are organized such that the contours and surface cell potential maps at a given bias voltage appear horizontally across two consecutive pages.

The two contou plots [figures G-1(a) and G-1(b), appendix G] show that the sheath, which propagates from the pinhole, looks like a narrow ring of charge at 75-volt potential. The corresponding surface potential maps [figures G-1(c) and G-1(d)] show nothing out of the ordinary. At 100-volt potential the contour plots [figures G-2(a) and G-2(b)] show only a slight expansion in sheath size. However, the corresponding surface cell potential maps [figure G-2(c)] for the first time show that the potential on the pinhole's nearest neighboring surface cells has undergone a sign change. The voltage on these cells has changed from something under -1 volt to something in the range of +1 volt. This appears to be the first evidence that "snapover" has begun. Next, at 130-volts potential figures G-3(a) and G-3(b) of appendix G show that the sheath edge has grown considerably. The x-y cross-sectional view [figure G-3(b)] shows that the sheath boundary has begun to wrap around the object past the front surfaces. Figure G-3(c) demonstrates that snapover is indeed occurring. The surface cell potentials of adjacent, nearest neigh oring cells have increased greatly. This coincides with the sharp change in current predicted by the NASCAP/LEO curve (figure f-6, curve d of appendix F) between 100-volts and 130-volts potential. By 600-volts potential, it is evident that the sheath edge (zero-potential contour line) completely surrounds the object [x-y view, figure G-4(b)] and that the 0.1-volts potential contour line (same view) wraps around three sides of the object. The surface cell potentials [figure G-4(c)] at this point are nearly all positive, except for the concentric ring of cells about the center and each of the surface cells on the right- and left-hand sides of the pinhole which are still between -1-volts and 0-volts potential. Evidently, secondary electron focusing, due to the applied field, seem to be the cause here. All other surface cells outside of the subdivided region [figure G-4(d)] still appear to be at a small negative potential. At 620-volts potential, the +0.1-volts potential contour line has completely snapped around the object [figure G-5(b)]. The zero-volt potential contour line [figure G-5(a)] appears to start growing along the length of the cylinder outward from the pinhole center. In figure G-5(c) the surface cell potential map at 620-volts potential clearly demonstrates that most surface cells within the subdivided region have dramatically increased in potential. This coincides with the sharp jump in current collection between 600 and 620 volts on the NASCAP/LEO predicted I-V curve. All surface cells outside of the subdivided

region, however, still remain at a small negative potential. At 680-volts potential there appears to be no significant change in either the contour plots or surface cell potential maps [figures G-6(a), G-6(b), G-6(c), and G-6(d), appendix G]. Finally, figures G-7(a) and G-7(b) show significant changes in sheath structure. It seems that the pinhole at this point begins to collect current like a larger bare sphere, as borne out by figures G-7(a) and G-7(b) and the NASCAP/LEO I-V curve at this voltage. It is also evident from figures G-7(c) and G-7(d) that considerable changes have taken place here also. For the first time we see that the surfaces of two cells on the top and bottom faces of the cable (outside the subdivided region) are beginning to grow to a substantial positive potential. This appears to account for the observed current shift between 680-volts and 685-volts potential.

Although there are no sharp changes in the current collected by the NASCAP/LEO I-V curve for the voltage range 690 through 1000 volts, for the sake of completeness, plots are presented in the 800- and 1000-volt potential region. At 800-volts potential, figure G-8(d) shows that the cell potentials of two adjacent cells (one cell flanking each side of the subdivided region on the front face of the cable) have charged to a slightly positive potential. This indicates that a positive charge sheath is beginning to grow over these surfaces along the length of the cable. The 1000-V surface cell potential map [figure G-9(d)] shows the same features with the only difference being that the voltage of the two adjacent cells has greatly increased.

CONCLUSIONS

The NASCAP/LEO I-V curve (appendix F, figure f-6) demonstrates that there are a number of different types of "snapover effects" occurring throughout the applied voltage range (as opposed to just one type that occurs throughout the entire pinhole bias voltage region as previously thought). Indeed, three such snapover effects were found in the present cable simulation and there could conceivably be more at higher bias voltages. (At 1000-volts potential, the majority of surface cells outside the subdivided region remain at approximately -1-volt potential. Therefore, at some higher potential it is conceivable that when all insulated surface cells become charged positive, there could be yet another large shift in current collection.) It is also conceivable that probe geometry, sharp edges, and pinhole size could have an effect on the exact number of snapover effects observed.

The first observed type of snapover effect occurs between 100 and 130 volts where the charge sheath first jumps to the insulator surfaces in the adjacent vicinity of the pinhole. This is probably due to the onset of significant secondary electron emissions in this voltage region.

The second type of snapover effect occurs between 600 and 620 volts, where the positive charge sheath in space completely surrounds the radius of the cable (as evidenced by the x-y view of the +0.1 contour line in figure G-5(b) of appendix G). The second type of snapover effect appears to be a necessary precursor to the third type of snapover effect observed.

The third and final type of snapover effect seems to be an edge effect occurring between 680- and 685-volts potential. It is here where the positive charge sheath has propagated from the front face to the sides of the cable and so is termed the "snap-around effect." In a perfect cylindrical cable, which has no sharp edges, this effect would probably not be seen until the positive surface charge sheath has completely wrapped around the cylinder. One must also conclude from the surface potential maps and the resultant NASCAP/LEO I-V curve that the positive surface charge sheath must snap around the cable before it can grow along its length.

Particularly disturbing is the lower voltage region (0- to 100-volts potential) where NASCAP/LEO predicts about a factor of 4 lower current than any of the Langmuir-type pinhole models (LTPM). Because NASCAP/LEO and the LTPMs solve Poission's equation, and since "snapover-type effects" are not applicable at lower voltages, it was assumed that the NASCAP/LEO predicted values would yield the same result as the LTPMs. The reason that they do not agree is that the NASCAP/LEO simulation assumes space charge limited currents where, in fact, the LTPMs have shown the current collection to be orbit limited. For the case where the Debye length is greater than the pinhole dimensions, many of the particles traced through the sheath boundary will miss the pinhole completely. As a result, less current is predicted by the current NASCAP/LEO simulations than by the LTPM approximations.

Langmuir-type probe models that attempt to bracket NASCAP/LEO current solutions, for an insulated cable with a pinhole, appear to suggest that current collection should favor an orbit limited current calculation. Furthermore, for small object dimensions (on the order of a centimeter), it is evident that at lower voltages LTPMs more accurately predict collected current, because NASCAP/LEO only makes its calculations in the space charge limited current regime.

Overall, (all low-voltage behavior aside), the Langmuir-type models (LTM) do quite well in bracketing the current collected by an insulated cable with a pinhole. Specifically, here the bare spherical and hemispherical LTM approximations, while they are not able to predict the sharp changes in current observed in the NASCAP/LEO-generated I-V curve, are within a factor of 4 of those values. The reason for this is clear. No bare probe model, however sophisticated, can hope to include secondary electron emission from the dielectric. Consequently, it is impossible for a bare probe model to predict snapover effects. Even so, the bare LTM approximations of the aforementioned geometries offer a reasonably good estimate of the current for a biased insulated probe with a pinhole without the need to resort to a number of lengthy NASCAP/LEO computer runs. For this reason they are quite useful. Such models have also been useful in understanding NASCAP/LEO results.

REFERENCES

Chen, F. F., "Electric Probes," Plasma Diagnostic Techniques, edited by R. H. Huddlestone and S. L. Leonard--Pure Applied Physics, Vol. 21, Academic Press, New York, 1965, chapter 4, pp. 113-200.

Cole, R. K., Ogawa, H. S., and Sellen, J. M., Jr., "Operation of Solar Cell Arrays in Dilute Streaming Plasmas," TRW Systems, Redondo Beach, Calif., TRW-09357-6006-R000, March 1968. (NASA CR-72376.)

Grier, N. T. and McKinzie, D. J., Jr., "Current Drainage to a High Voltage Probe in a Dilute Plasma," NASA TMS 67890, 1971.

International Dictionary of Physics and Electronics, 2nd Ed., D. Van Nostrand Company, Inc., Princeton, New Jersey, p. 1060, 1961.

Katz, I., et al., "A Three Dimensional Dynamic Study of Electrostatic Charging in Materials," (SSS-R-3367), Systems, Science and Software (NASA Contract NAS 20119) NASA CR-13526, August 1977.

Kennerud, K. L. "High Voltage Solar Array Experiments," NASA CR-121280, 1974.

Langmuir and Blodgett, "Currents Limited by Space Charge Between Concentric Spheres," Physical Review, Vol. XXII, 49, July 1924.

Langmuir and Blodgett, "Currents Limited by Space Charge Between Coaxial Cylinders," Physical Review, Vol. XXII, 347, October 1923.

Mandell, M. J., Jongeward, G. A., and Katz, I., "NASCAP/LEO Reference Manual," SSS-R-85-7300, NASA Contract Report pp. 4-9, June 1985.

Meulenberg, A., Robinson, Jr., "Conduction Through Punctures in Metal Backed Dielectrics," 3rd Spacecraft Charging Technology Conference, Colorado Springs, Colorado, November 1980, pp. 342-352.

Parker, L. W., "Plasma-Photosheath Theory for Large High-Voltage Space Structures," Progress in Aeronautics and Astronautics, Vol. 71, New York, New York, American Institute of Aeronautics and Astronautics (edited by Garrett and Pike), 1980.

Reitz, J. R. and Milford, F. J., Foundations of Electromagnetic Theory, Reading, Maine, Addison-Wesley Publishing Company, 2nd Ed., 1969, pp. 269-292.

Snyder, D. B., "Discharges on a Negatively Biased Solar Cell Array in a Charge-Partical Environment," 4th Spacecraft Environmental Interactions Conference, Colorado Springs, Colorado, October 1983, pp. 379-388.

Staskus, J. A., "Electron Beam Charging of Space Shuttle Thermal Protection System Tiles." 4th Spacecraft Environmental Interactions Technology Conference, Colorado Springs, Colorado, October 1983, pp. 91-102.

Stevens, N. J., "Interactions Between Spacecraft and the Charged Particle Environment," 2nd Spacecraft Charging Technology Conference, Colorado Springs, Colorado, October 31 - November 2, 1978, pp. 276-277.

Stevens, N. J., et al., "Investigation of High Voltage Spacecraft System Interactions with Plasma Environments," NASA TM-78831, 13th Electronic Propulsion Conference, San Diego, California, 1978.

LIST OF APPENDICES

APPENDIX A	Fig. A-1	NASCAP/LEO Object (full view)
	Fig. A-2	NASCAP/LEO Object (subdivided region with pinhole)
APPENDIX B	Calculations for the radius of a sphere of equal surface area to the pinhole in NASCAP/LEO defined object.	
APPENDIX C	Calculations for radius of a hemisphere of equal surface area to the pinhole in NASCAP/LEO defined object.	
APPENDIX D	Table D-1	Space charge limited equations for a parallel plate, concentric spheres and hemispheres, coaxial cylinders.
APPENDIX E	Table E-1	Determination of space charge limited or orbit limited currents for planes, spheres, cylinders, and hemispheres.
APPENDIX F	Fig. F-1	Plot of V versus R_0,P for bare cylindrical probes using a planar sheath geometry for R_0.
	Fig. F-2	Plot of V versus R_0,P for bare cylindrical probes using a cylindrical sheath geometry for R_0.
APPENDIX G	Fig. F-3	Plot of V versus R_0,P for bare spherical probes using a planar sheath geometry for R_0.
	Fig. F-4	Plot of V versus R_0,P for bare spherical probes using a spherical sheath geometry for R_0.
	Fig. F-5	Plot of V versus R_0,P for bare hemispherical probes using a hemispherical sheath geometry for R_0.
	Fig. F-6	Comparison of collected currents between various Langmuir-type probe models and NASCAP/LEO values.
APPENDIX G	Figs. G-1(a), G-1(b) G-1(c), & G-1(d)	75-volt contour plots and surface cell potential maps.
	Figs. G-2(a), G-2(b) G-2(c), & G-2(d)	100-volt contour plots and surface cell potential maps.
	Figs. G-3(a), G-3(b) G-3(c), & G-3(d)	130-volt contour plots and surface cell potential maps.
	Figs. G-4(a), G-4(b) G-4(c), & G-4(d)	600-volt contour plots and surface cell potential maps.

APPENDIX G (continued)	Figs. G-5(a), G-5(b) G-5(c), & G-5(d)	620-volt contour plots and surface cell potential maps.
	Figs. G-6(a), G-6(b) G-6(c), & G-6(d)	680-volt contour plots and surface cell potential maps.
	Figs. G-7(a), G-7(b) G-7(c), & G-7(d)	685-volt contour plots and surface cell potential maps.
	Figs. G-8(a), G-8(b) G-8(c), & G-8(d)	800-volt contour plots and surface cell potential maps.
	Figs. G-9(a), G-9(b) G-9(c), & G-9(d)	1,000-volt contour plots and surface cell potential maps.

APPENDIX A

CYLINDRICAL OBJECT WITH A PINHOLE

XMESH = 1/8 in. = .093175 METERS

DIMENSIONS:	X	Y	Z		
	1	1	30	KAPTON	120 SURFACE CELLS (-2 CELLS IN SUBDIVIDED REGION)

SUBDIVIDED REGION:	X	Y	Z		
(2 SURFACE CELLS)	0	8	16	KAPTON	124 SURFACE CELLS
(PINHOLE)		2	2	GOLD	4 SURFACE CELLS

OBJECT FULL VIEWS:

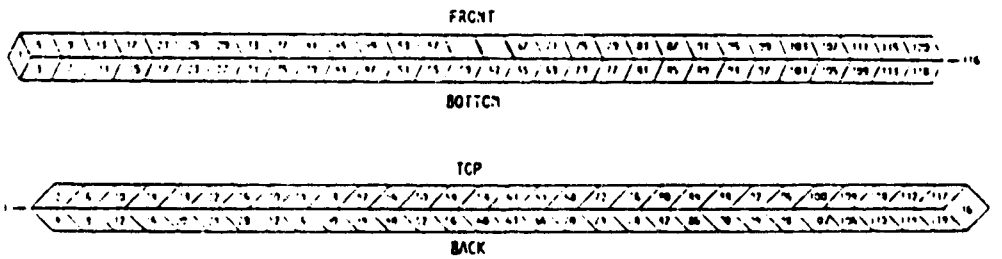

FIGURE A-1.

SUBDIVIDED REGION (EXPANDED VIEW):

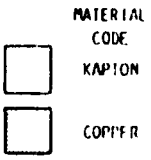

229	230	231	232	233	234	235	236	237	238	239	240	241	242	243	244
213	214	215	216	217	218	219	220	221	222	223	224	225	226	227	228
197	198	199	200	201	202	203	204	205	206	207	208	209	210	211	212
181	184	185	186	187	188	189	247	248	190	191	192	193	194	195	196
169	170	171	172	173	174	175	245	246	176	177	178	179	180	181	182
153	154	155	156	157	158	159	160	161	162	163	164	165	166	167	168
137	138	139	140	141	142	143	144	145	146	147	148	149	150	151	152
121	122	123	124	125	126	127	128	129	130	131	132	133	134	135	136

FIGURE A-7.

APPENDIX B

XMESH = 1/8 IN. = 3.175×10^{-3} METERS

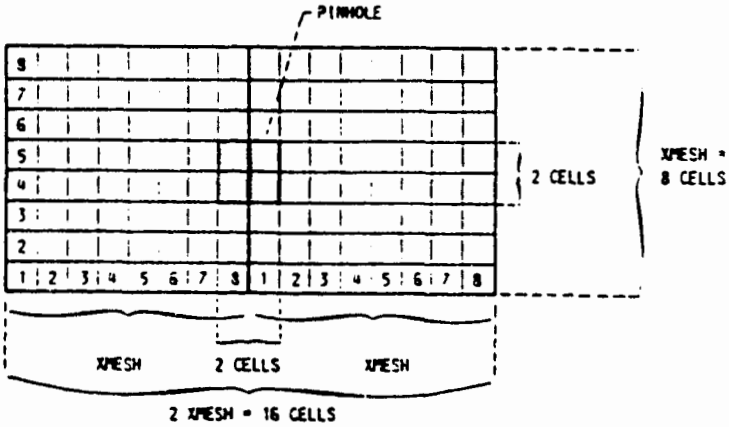

TOTAL NUMBER OF CELLS IN SUBDIVIDED REGION = 8 x 16 = 128 CELLS

TOTAL NUMBER OF CELLS IN PINHOLE = 4 CELLS

TOTAL SURFACE AREA OF SUBDIVIDED REGION = $S.A._{SUBD}$ = (2) (XMESH) (XMESH)

SURFACE AREA OF PINHOLE = $S.A._{PIN} = \frac{4}{128}$ (2) $(XMESH)^2$

SURFACE AREA OF SPHERE = $S.A._{PIN} = 4\pi a^2$; a_{SPH} = SPHERE RADIUS

$S.A._{SPH} = S.A._{PIN}$

FINDING RADIUS (a) OF A SPHERE OF EQUAL SURFACE AREA TO THAT OF THE PINHOLE IN NASCAP/LEO OBJECT:

$S.A._{PIN} = 4\pi a^2$

$$a_{SPH} = \sqrt{\frac{S.A._{PIN}}{4\pi}} = \frac{XMESH}{8\sqrt{\pi}} = 2.23912 \times 10^{-4} \text{ METERS}$$

FIGURE B-1.

APPENDIX C

FINDING THE RADIUS OF A HEMISPHERE (a_{HEM}) OF EQUAL SURFACE AREA TO A SPHERE OF RADIUS (a_{SPH})

SURFACE AREA OF SPHERE = $S.A._{SPH}$

SURFACE AREA OF HEMISPHERE = $S.A._{HEM}$

LET:

$$S.A._{SPH} = S.A._{HEM} = S.A._{PIN}$$

THEN:

$$\left.\begin{aligned} S.A._{SPH} &= 4\pi a^2_{SPH} \\ S.A._{HEM} &= 2\pi a^2_{HEM} \end{aligned}\right\} \quad \text{WHERE:} \quad S.A._{PIN} = \frac{XMESH^2}{16}$$

THEREFORE:

$$a_{SPH} = \frac{XMESH}{8\sqrt{\pi}} \quad \text{AND} \quad a_{HEM} = \frac{XMESH}{4\sqrt{2\pi}}$$

$$\frac{a_{HEM}}{a_{SPH}} = \sqrt{2} \quad \text{OR} \quad a_{HEM} = \sqrt{2}\ a_{SPH} = 3.16659 \times 10^{-1}\ \text{METERS}$$

FIGURE C-1.

APPENDIX D

BARE PROBE GEOMETRY	I CURRENT (AMPS)	j_r * RANDOM THERMAL CURRENT DENSITY (A/m^2) $= Ne\sqrt{\frac{kTe}{2\pi m}}$	THICK SHEATH r_o APPROXIMATION SPACE CHARGE SHEATH RADIUS (METERS) $R_o = r_o + a$
II FLAT PLATES:	CHEN: (1.a) ✓ $I = j_r$	CHILD (1.b) ✓ * $j_r = \frac{4\varepsilon_o}{9}\sqrt{\frac{2e}{m}}\frac{V^{3/2}}{r_o^2}$	S-CUBED (1.c) * $r_o = \underbrace{\left[\left(\frac{8\varepsilon_o}{9e}\right)^2 \pi\right]^{1/4}}_{9330} \frac{V^{3/4}}{\sqrt{N}(kT)^{1/4}}$
CONCENTRIC SPHERES:	CHEN: (2.a1) ✓ $I = 4\pi r_o^2 j_r$ LANGUIR: (2.a2) $I = \frac{4\sqrt{2}\varepsilon_o}{9}\sqrt{\frac{e}{m}}\frac{V^{3/2}}{a^2}$ SMALLER SPHERE KENNERUDE: (2.a3) $a^2 = 1.16\,(r_o/a)^{3/2}$	(2.b) ✓ * $j_r = \frac{\varepsilon_o}{9\pi}\sqrt{\frac{2e}{m}}\frac{V^{3/2}}{r_o^2 a^2}$	(2.c) * $r_o = \underbrace{\left[\frac{2\varepsilon_o}{\sqrt{109\,\pi}e}\right]^{2/7}}_{86.31} \frac{(aV)^{3/7}}{N^{2/7}(kT)^{1/7}}$
COAXIAL CYLINDERS:	LANGMUIR: (3.a1) ✓ $I = 2\pi r_o \ell j_r$ (3.a2) $I = 8\pi\ell\varepsilon_o\sqrt{\frac{e}{m}}\frac{V^{3/2}}{r_o(\ln r_o/a)^2}$	(3.b) ✓ * $j_r = \frac{4\varepsilon_o}{9}\sqrt{\frac{2e}{m}}\frac{V^{3/2}}{r_o^2(\ln r_o/a)^2}$	(3.c) * $r_o \ln(r_o/a) = \underbrace{\left[\left(\frac{8\varepsilon_o}{9e}\right)^2 \pi\right]^{1/4}}_{9330} \frac{V^{3/4}}{\sqrt{N}(kT)^{1/4}}$
CONCENTRIC HEMISPHERES: NOTE: a IS THE SAME VALUE FOR SPHERES AND HEMISPHERES.	(4.a1) ✓ $I = 2\pi r_o^2 j_r$ (4.2) $I = 4\sqrt{2}\varepsilon_o\sqrt{\frac{e}{m}}\frac{V^{3/2}}{a^2}$ LARGER SPHERE (4.3) $a^2 = 1.16\,(r_o/\sqrt{2}a)^{3/2}$	(4.b) ✓ * $j_r = \frac{2\varepsilon_o}{9\pi}\sqrt{\frac{2e}{m}}\frac{(\sqrt{2}aV)^{3/2}}{r_o^2 a^2}$	(4.c) * $r_o = \underbrace{\left[\frac{4\varepsilon_o}{\sqrt{109\,\pi}e}\right]^{2/7}}_{105.21} \frac{(\sqrt{2}aV)^{3/7}}{(N)^{2/7}(kT)^{1/7}}$

APPENDIX D. TABLE 1 - (ALL SPECIFIED RELATIONS ARE IN MKS UNITS. ✓ THESE RELATIONS ARE FOR ELECTRONS OF MASS m FOR IONS MULTIPLY R.M.S. OF CURRENT BY $\sqrt{\frac{m}{M}}$: M BEING THE MASS OF THE IONS. *ALL VALUES OF kT ARE IN UNITS OF eV).

APPENDIX E

(5.0) p = IMPACT PARAMETER, cm = $a\sqrt{1 + \frac{qV}{\mathcal{E}}}$

V = APPLIED VOLTAGE

r = SPACE CHARGE SHEATH RADIUS, m

E = ENERGY IN, eV = kT

j_r = RANDOM THERMAL CURRENT DENSITY, amps/m^2

a = PROBE RADIUS, m

ℓ = PROBE LENGTH, m

q = ELECTRONIC OR IONIC CHARGE

TABLE 2

ORBIT LIMITED CURRENT	$P < R_0 < P$	SPACE CHARGE LIMITED CURRENT
(5.3b) ———	PLANAR GEOMETRY	$I = j_r$ (5.1a)
(5.2b) $I = 4\pi P^2 j_r$	SPHERICAL GEOMETRY	$I = 4\pi R_0^2 j_r$ (5.2a)
(5.4b) $I = 2\pi P \ell\ j_r$	CYLINDRICAL GEOMETRY	$I = 2\pi R_0\ \ell j_r$ (5.3a)
(5.4b) $I = 2\pi P^2\ j_r$	HEMISPHERICAL GEOMETRY	$I = 2\pi R_0^2\ j_r$ (5.4a)

FIGURE E-1.

APPENDIX F

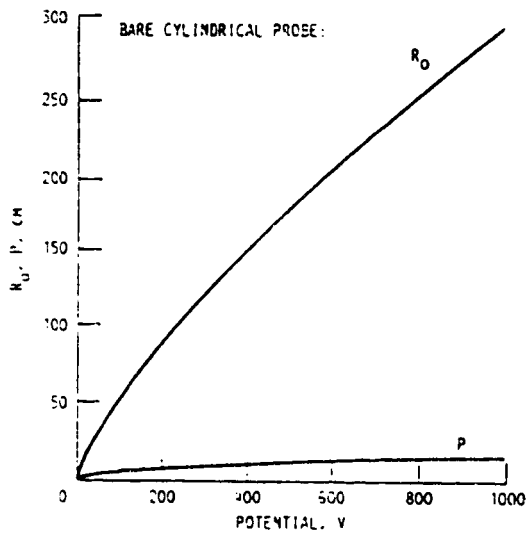

FIGURE F-1. - PLANAR CHARGE SHEATH APPLIED TO A CYLINDRICAL PROBE GEOMETRY.

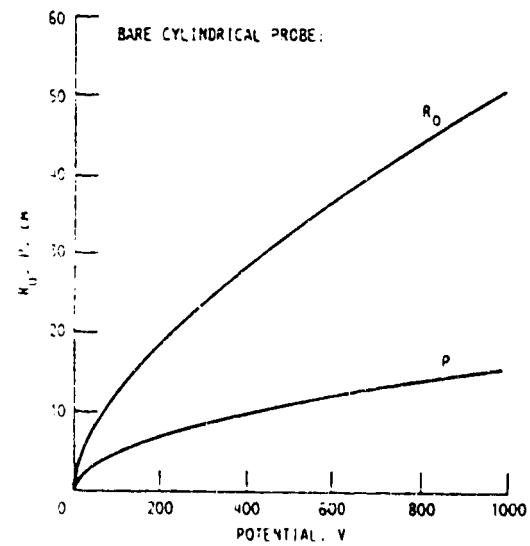

FIGURE F-2. - CYLINDRICAL CHARGE SHEATH APPLIED TO TO A CYLINDRICAL PROBE GEOMETRY.

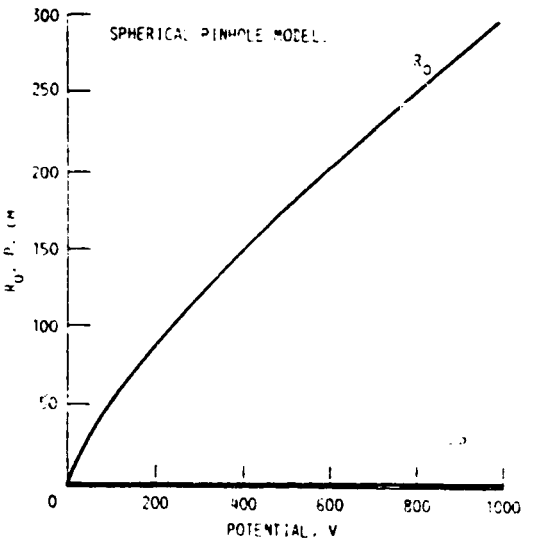

FIGURE F-3. - PLANAR CHARGE SHEATH APPLIED TO A SPHERICAL PINHOLE GEOMETRY.

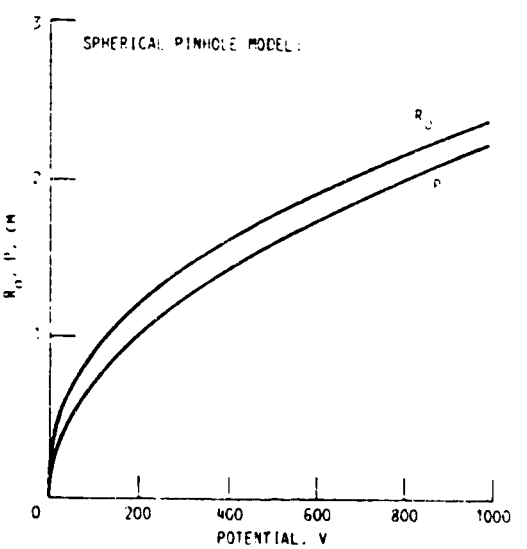

FIGURE F-4. - SPHERICAL CHARGE SHEATH APPLIED TO A SPHERICAL PINHOLE GEOMETRY.

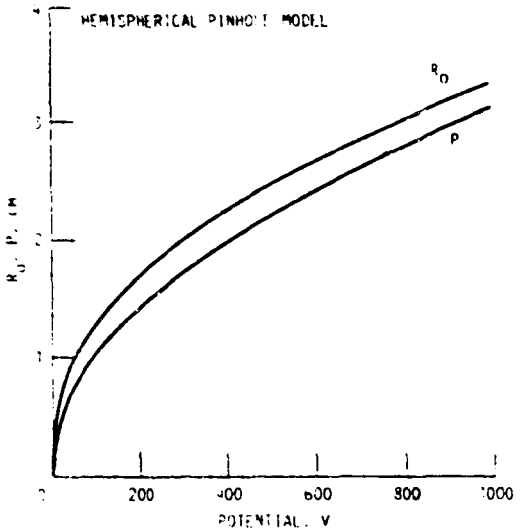

FIGURE 5-5. - HEMISPHERICAL CHARGE SHEATH APPLIED TO A HEMISPHERICAL PINHOLE GEOMETRY.

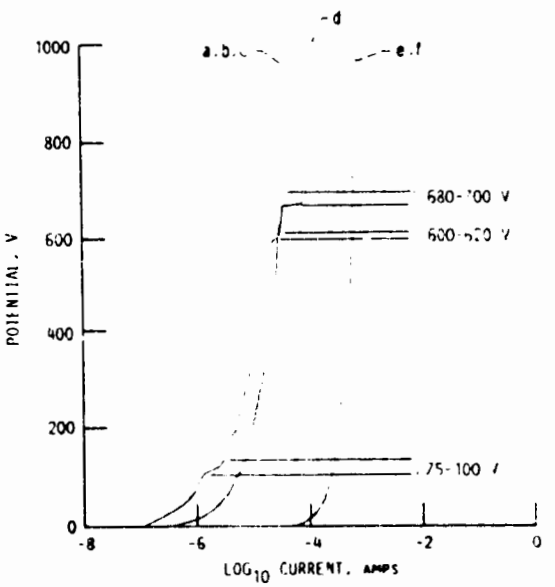

(a) ORBIT LIMITED CURRENT RESULTING FROM A PLANAR SPACE CHARGE SHEATH THICKNESS BEING APPLIED TO A SPHERICAL PINHOLE CURRENT

(b) ORBIT LIMITED CURRENT RESULTING FROM A SPHERICAL SPACE CHARGE SHEATH THICKNESS BEING APPLIED TO A SPHERICAL PINHOLE CURRENT

(c) ORBIT LIMITED CURRENT RESULTING FROM A HEMISPHERICAL SPACE CHARGE SHEATH THICKNESS BEING APPLIED TO A HEMISPHERICAL PINHOLE CURRENT

(d) NASCAP/LEO PREDICTED CURRENT FOR AN INSULATED CABLE WITH A SINGLE PINHOLE

(e) ORBIT LIMITED CURRENT RESULTING FROM A PLANAR SPACE CHARGE SHEATH THICKNESS BEING APPLIED TO A CYLINDRICAL PROBE CURRENT (SAME OVERALL DIMENSIONS AS NASCAP/LEO OBJECT)

(f) ORBIT LIMITED CURRENT RESULTING FROM A CYLINDRICAL SPACE CHARGE SHEATH THICKNESS BEING APPLIED TO A CYLINDRICAL PROBE CURRENT (SAME OVERALL DIMENSIONS AS NASCAP/LEO OBJECT)

FIGURE F-6.

APPENDIX G

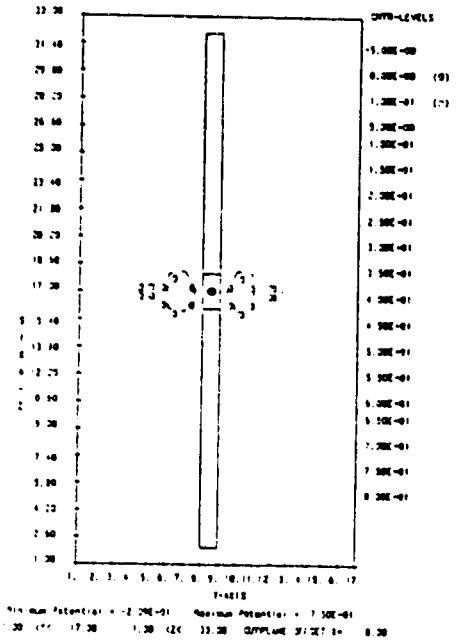

FIGURE G-1(a).

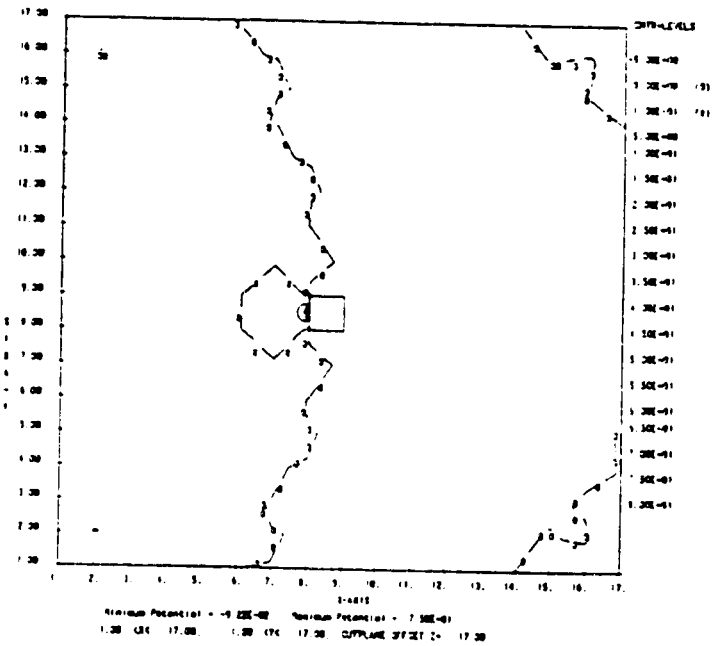

FIGURE G-1(b).

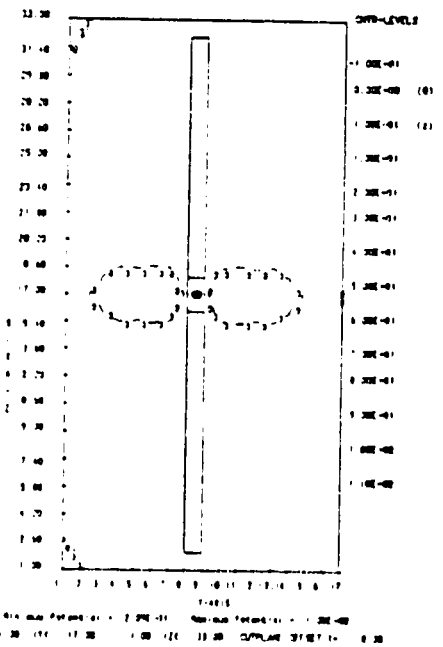

FIGURE G-2(a).

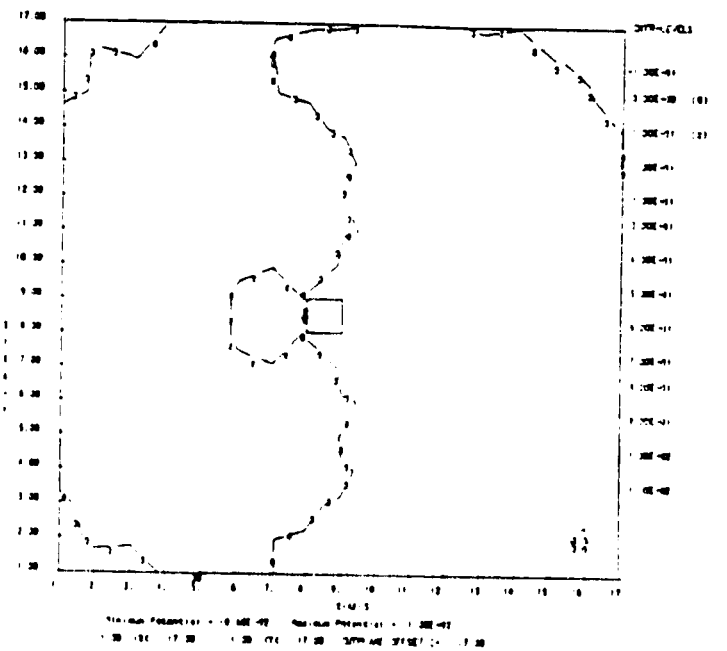

FIGURE G-2(b).

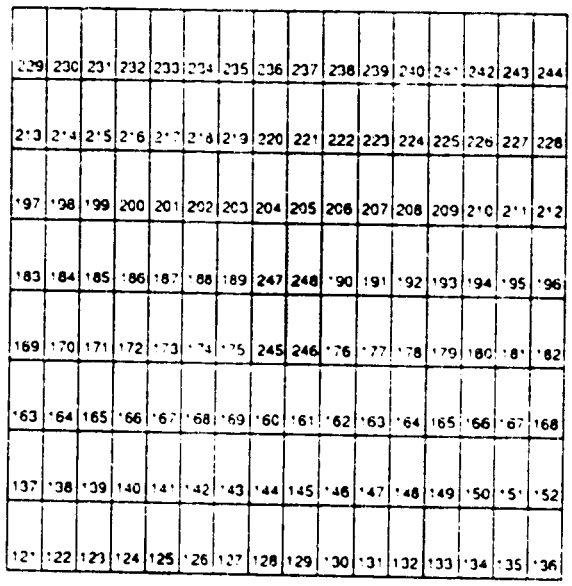

FIGURE G-1(c).

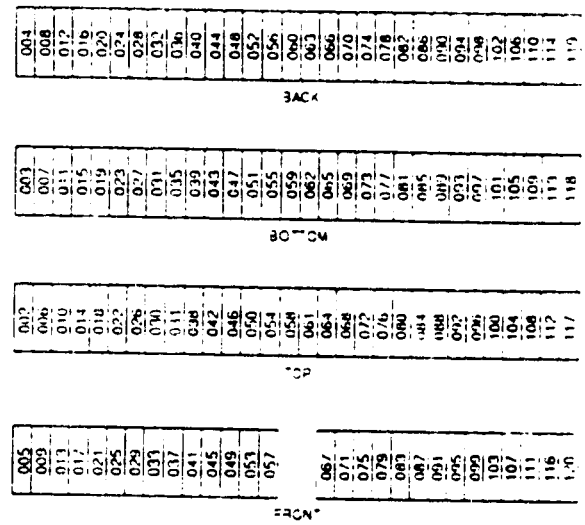

FIGURE G-1(d).

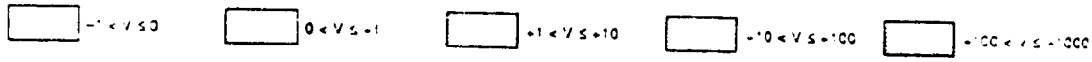

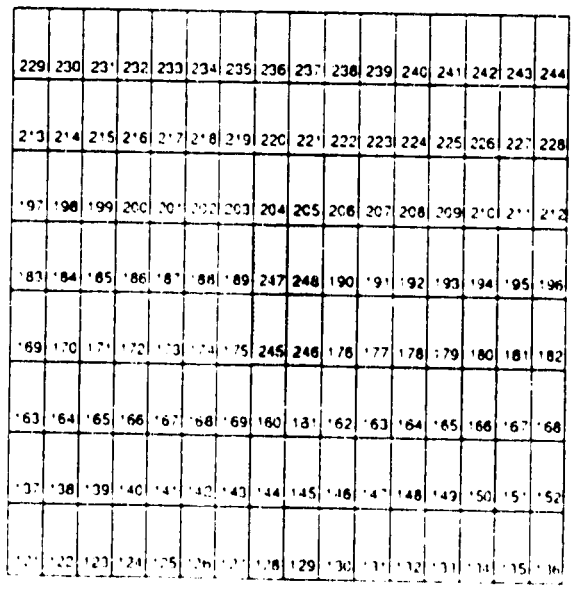

FIGURE G-2(c).

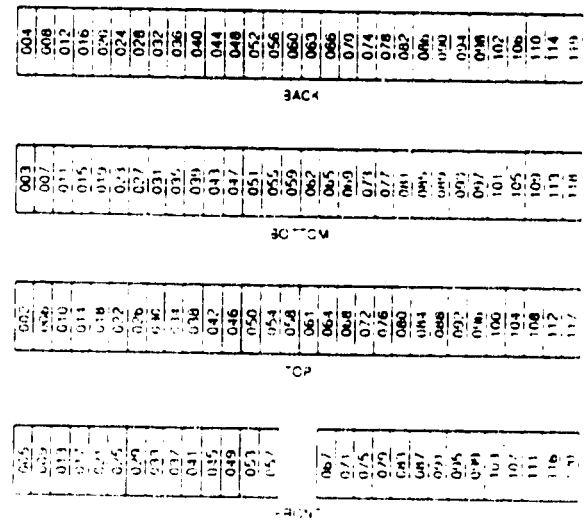

FIGURE G-2(d).

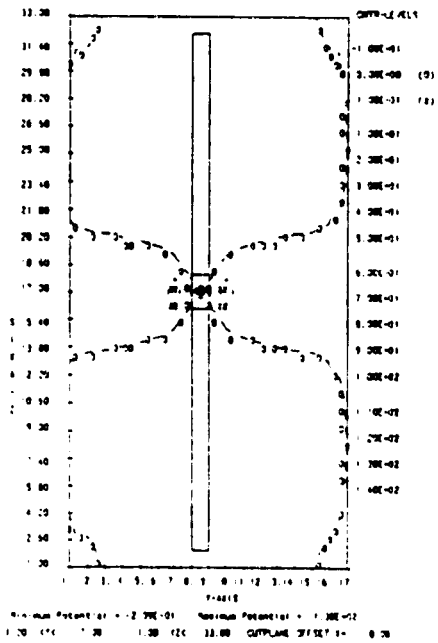

FIGURE G-3(a).

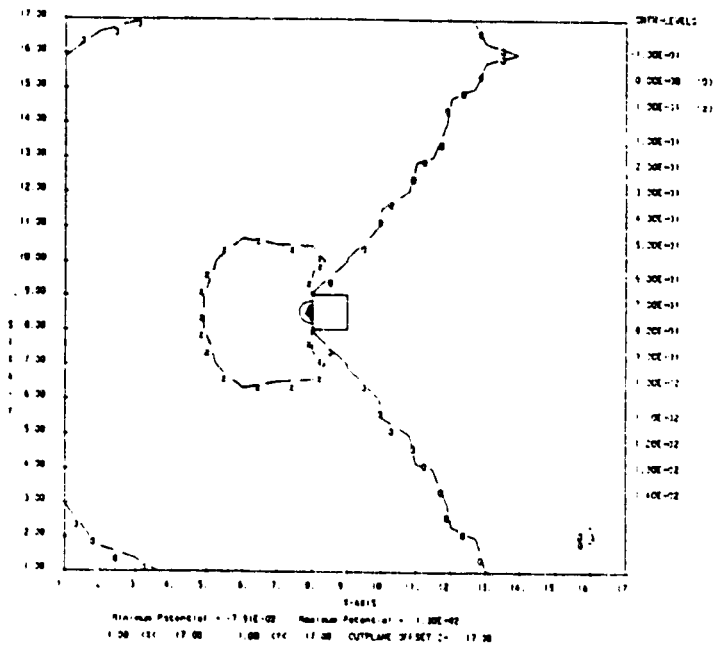

FIGURE G-3(b).

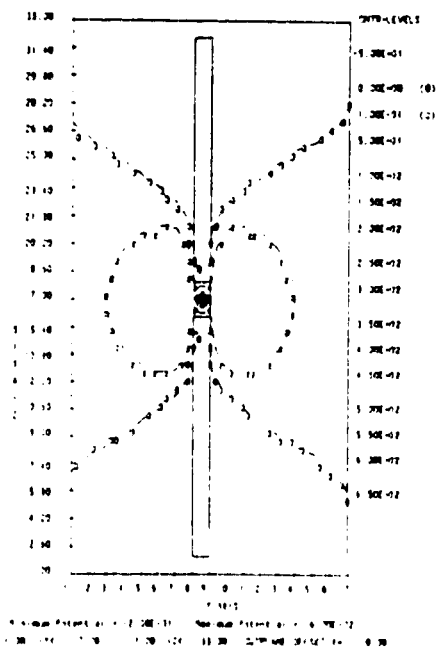

FIGURE

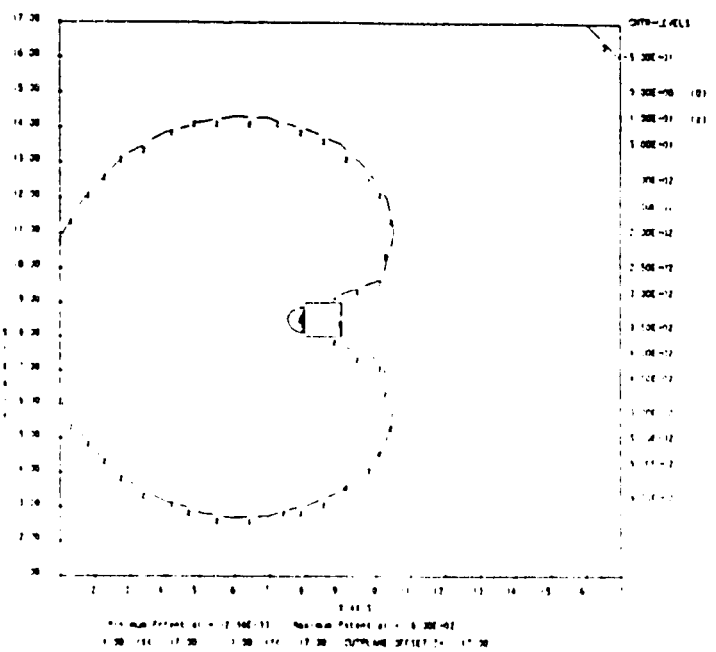

FIGURE

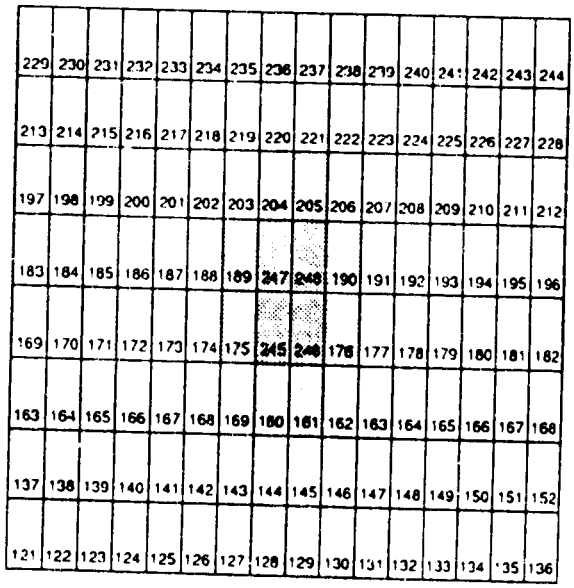

FIGURE G-3(c).

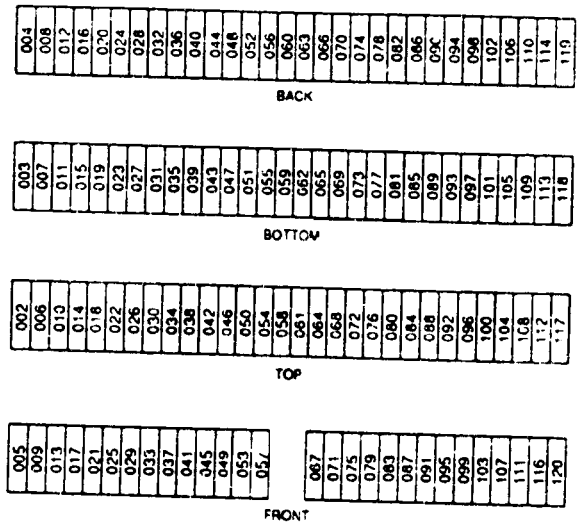

FIGURE G-3(d).

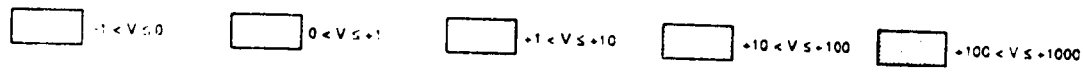

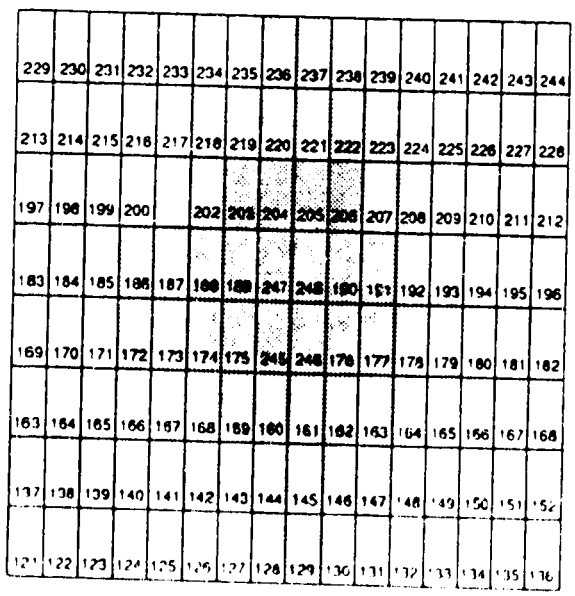

FIGURE G-4(c).

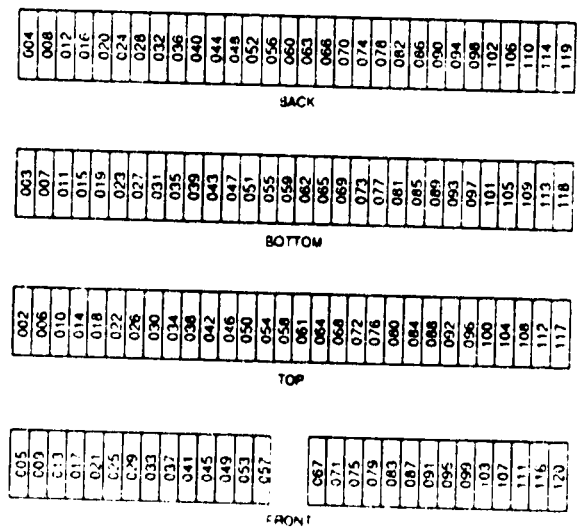

FIGURE G-4(d).

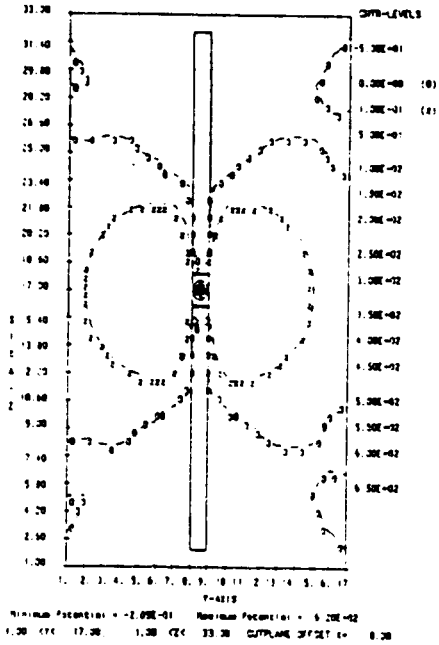

FIGURE G-5(a).

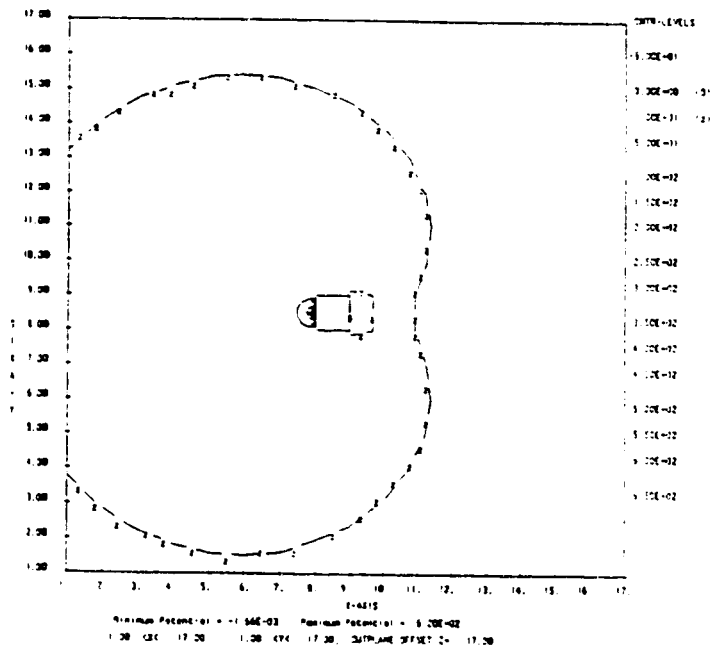

FIGURE G-5(b).

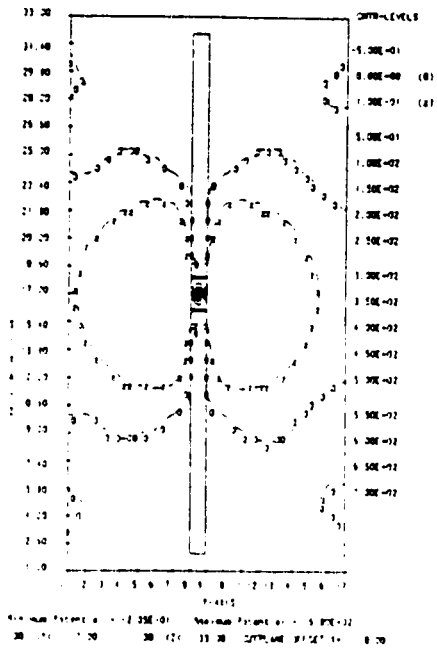

FIGURE G-5(c).

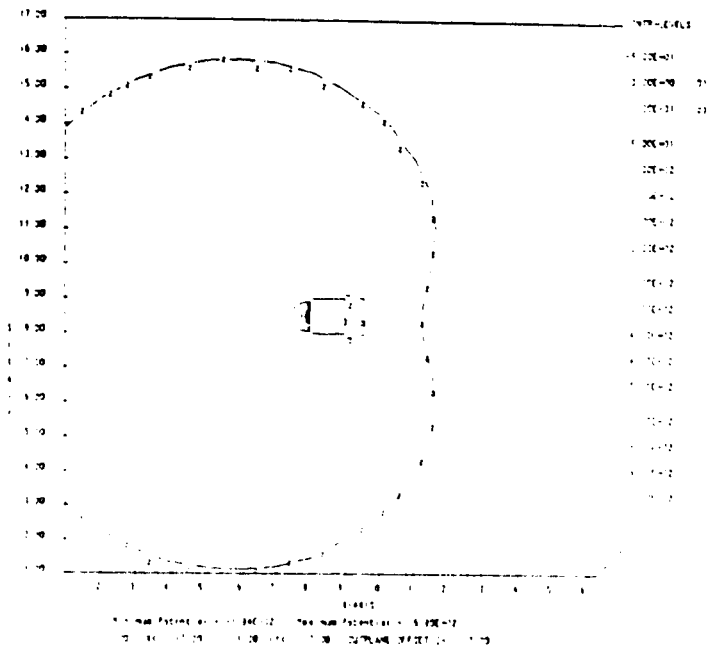

FIGURE G-5(d).

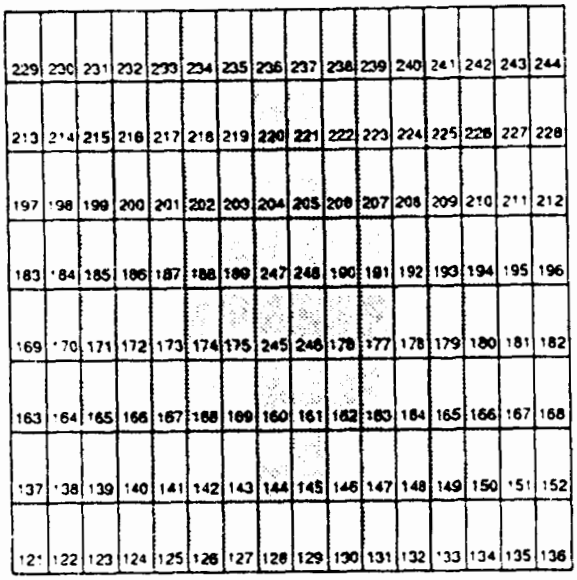

FIGURE G-5(C).

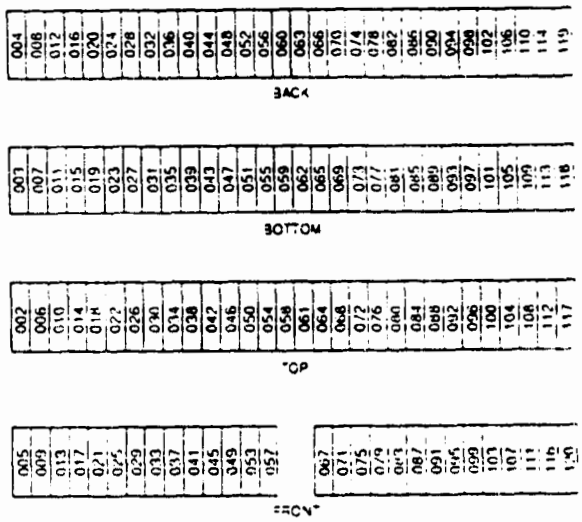

FIGURE G-5(D).

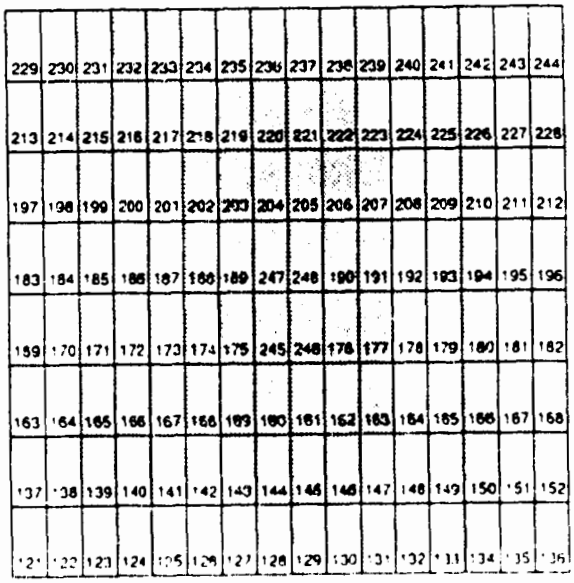

FIGURE G-5(C).

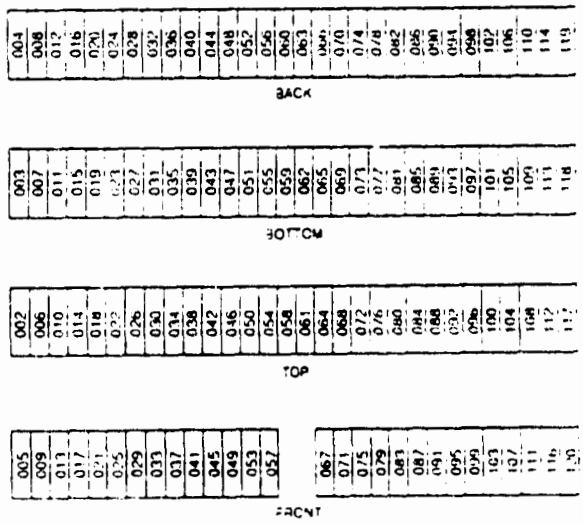

FIGURE G-5(D).

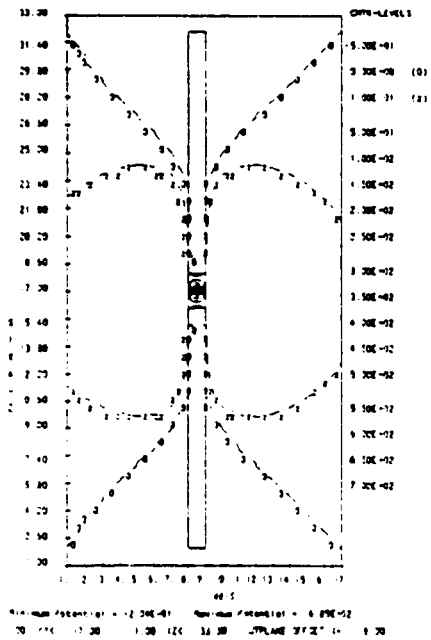

FIGURE G-7 a).

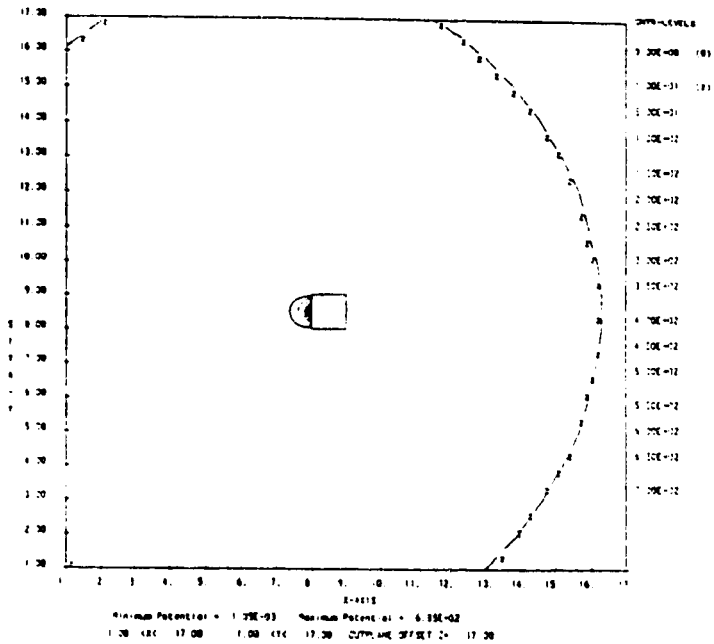

FIGURE G-7(b).

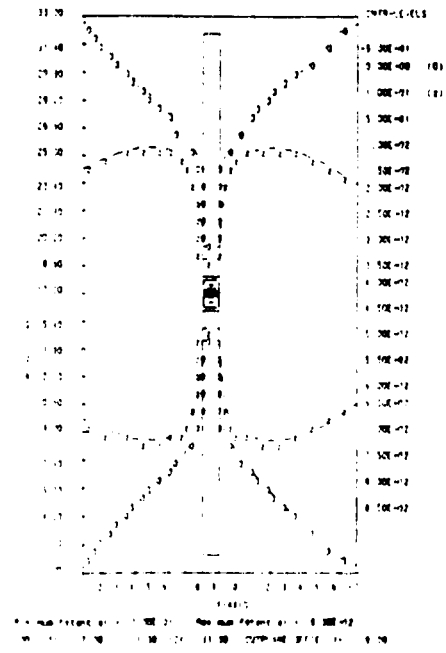

FIGURE G-8(a)

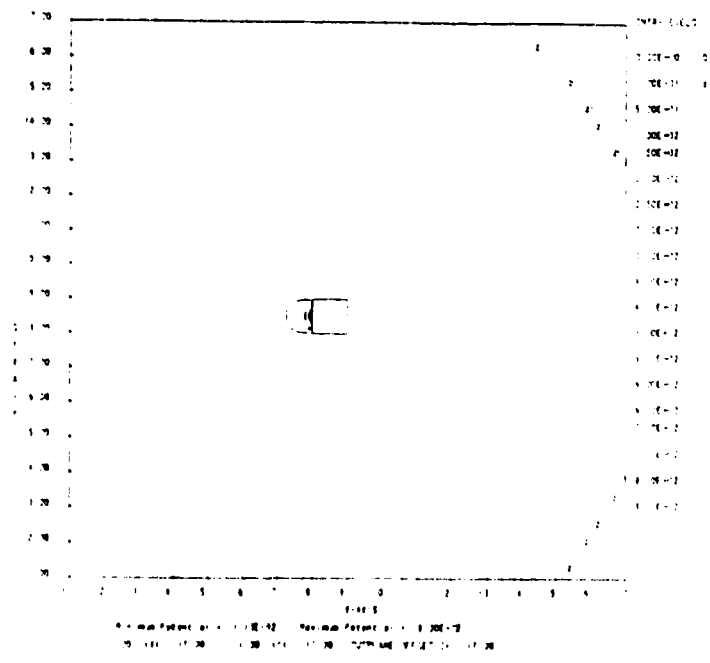

FIGURE G-8(b)

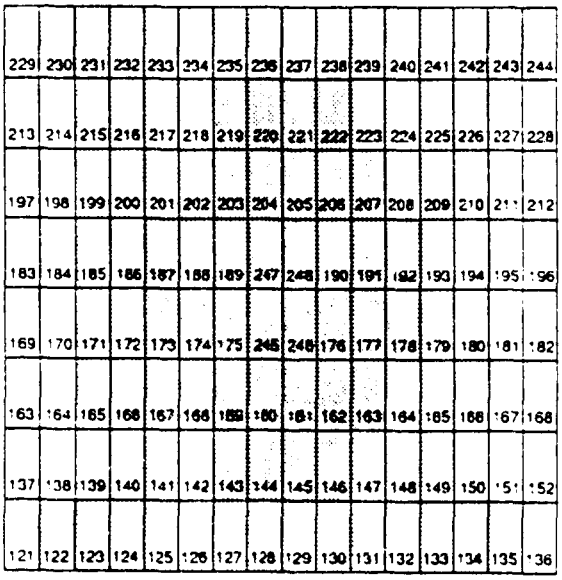

FIGURE 3-7(c).

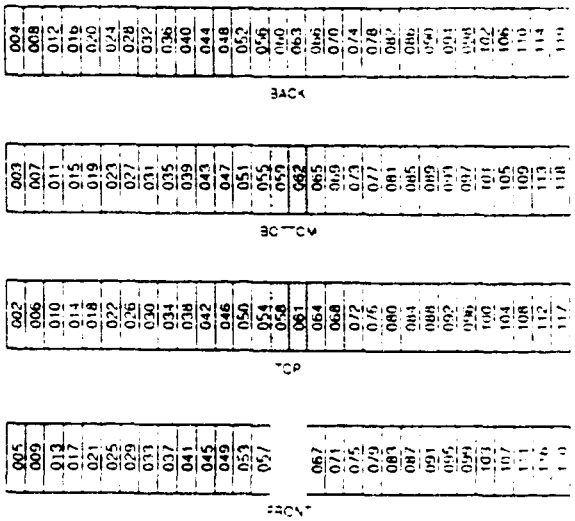

FIGURE 3-7(d).

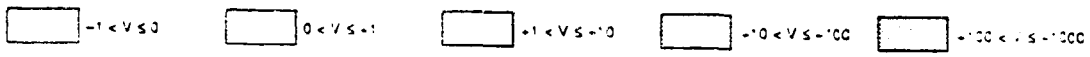

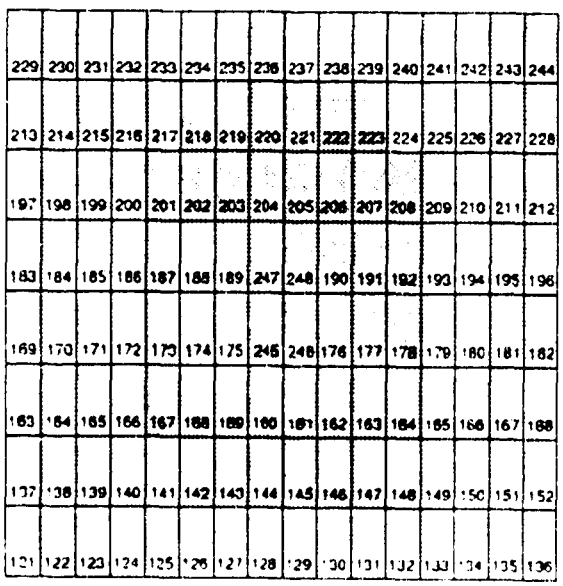

FIGURE 3-8(c).

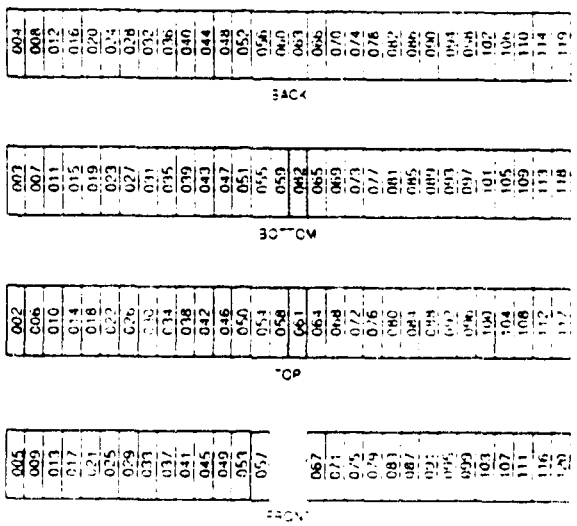

FIGURE 3-8(d).

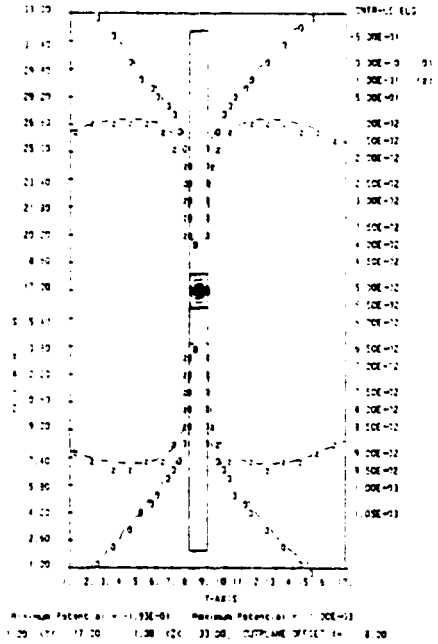

FIGURE G-9(a).

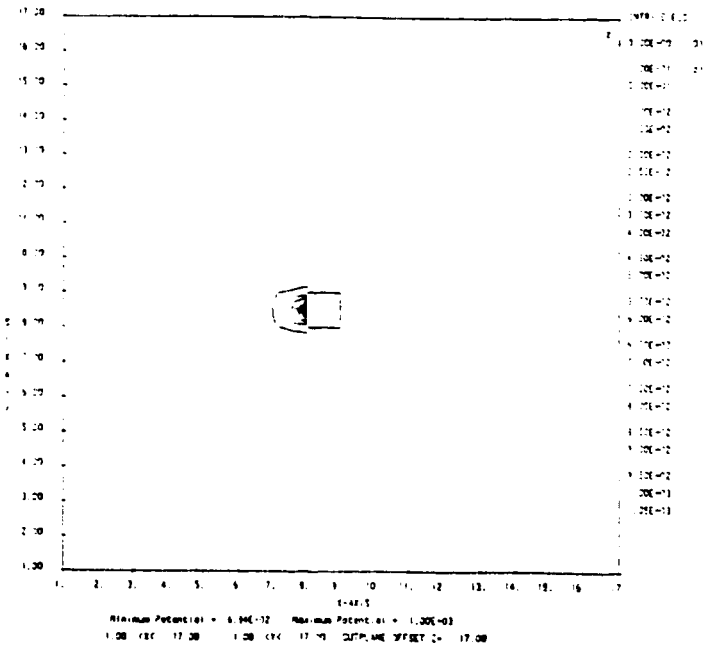

FIGURE G-9(b)

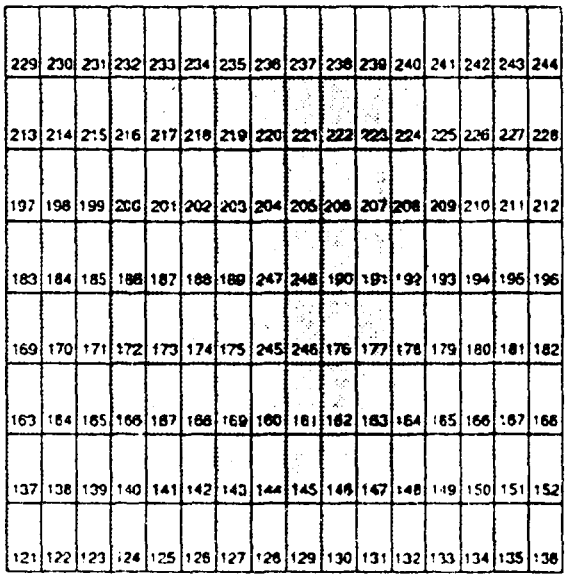

FIGURE G-9(c).

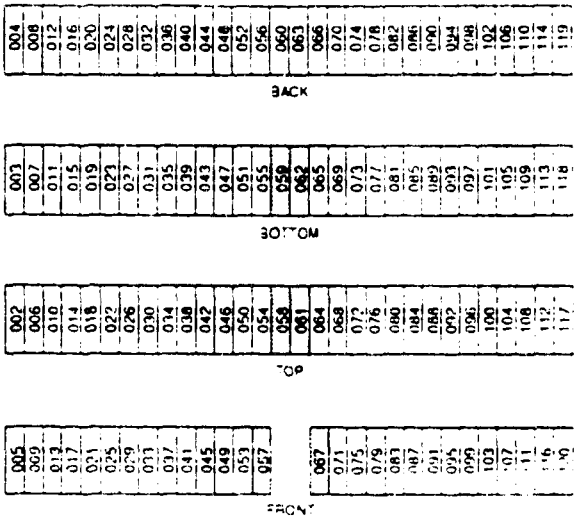
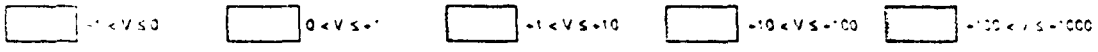
FIGURE G-9(d)